Electronic Supplementary Material (ESI) for Soft Matter.
This journal is © The Royal Society of Chemistry 2019

Supplementary Information

Evidence for water ridges at oil-water interfaces: implications for ion transport

Boyao Wen, Chengzhen Sun, Wenxiu Zheng, Bofeng Bai * and Eric Lichtfouse

State Key Laboratory of Multiphase Flow in Power Engineering, Xi'an Jiaotong University, Xi'an, Shaanxi 710049, China

* Author to whom correspondence should be addressed. Electronic mail: bfbai@mail.xjtu.edu.cn

Contents

1. Model and methods 1
1.1 Force field 1
1.1.1 TIP3P water model 1
1.1.2 OPLS All-Atom force field 2
1.1.3 Force field parameters for ions 3
1.2 Simulation details 4
1.3 Model validation 5
2. Microstructures 6
2.1 Typical cases of ion transfer 7
2.2 Water channel 8
2.3 Density distribution 11
2.4 Interfacial thickness 14
References 15

1. Model and methods

1.1 Force field

1.1.1 TIP3P water model

As the most important substance on Earth, water plays a key role in many biological, chemical, physical and industrial processes. With the development of computer simulation techniques, developing an accurate water model to predict the properties of water is an important subject of research. The complexity of the water properties combined with multiple possible approximation (e.g., quantum vs. classical, flexible vs. rigid) has led to the proposal of many computational models for water. [1-8] However, it is very difficult to choose the best potential model of water because every water potential model is often developed and applied for describing a specific property. Because of our regular simulation conditions, we choose TIP3P water model with a long-range Coulombic solver considering the effect of ions to simulate water molecules. In our previous work, [9, 10] we showed that this water model can accurately simulate the density and structures of water molecules at the interfaces. Meanwhile, the interfacial tension between decane and water phase is consistent with experimental values, reflecting the nice combination of decane potential and water model. In this study, we employ the TIP3P model, [11] which is proven to be efficient and can precisely predict the structure and dynamics of the water phase, to simulate the interactions between water molecules. The TIP3P model assigns the charge and LJ parameter for each atom of the water molecule. Additionally, the *harmonic* bond and angle style are utilized to describe the O-H bond and the H-O-H angle. In 1984, Price *et al.* [12] modified the parameters and developed the TIP3P model with a long-range Coulomnic solver, which can effectively

describe electrostatic interaction. The simulation parameters in our work are identical with those parameters modified by Price *et al*. [12] More detailed parameters can be found in **Table S1**.

1.1.2 OPLS All-Atom force field

In this paper, the OPLS All-Atom (OPLS-AA) force field [13] is utilized to mimic the interactions between decane molecules. Our previous simulation results prove its ability to accurately reproduce the thermodynamic and interfacial properties of decane, such as density, diffusion coefficients and interfacial tension. [9, 10] The non-bonded interactions, bond stretching, angle bending and torsion interactions are considered in this force field:

$$E = E_{ab} + E_{bond} + E_{angle} + E(\phi) \tag{S1}$$

The non-bonded interaction includes the standard 12/6 Lennard-Jones and Coulombic pairwise interactions, given by

$$E_{ab} = 4\varepsilon\left[\left(\frac{\sigma}{r_{ab}}\right)^{12} - \left(\frac{\sigma}{r_{ab}}\right)^{6}\right] + \frac{Cq_a q_b}{\chi r_{ab}} \qquad (r_{ab} < r_{cut}) \tag{S2}$$

where ε is the depth of the potential well, σ is the distance between atoms when the potential is zero, r_{cut} is the cutoff radius, C is an energy-conversion constant, q_a and q_b are the charges of atom a and b, χ is the dielectric constant. While r_{ab} is greater than r_{cut}, we only calculate the long-range electrostatic interactions by using the Particle-Particle Particle-Mesh (PPPM) method. Potential parameters between unlike atoms are obtained based on the Lorentz-Berthelot combining rule:

$$\sigma_{ij} = \frac{\sigma_{ii} + \sigma_{jj}}{2} \qquad \varepsilon_{ij} = \sqrt{\varepsilon_{ii}\varepsilon_{jj}} \tag{S3}$$

The bond stretching and angle bending in the molecule are described by the *harmonic* bond style, as follows:

$$E_{bond} = K_{bond}(r_{ab} - r_0)^2 \tag{S4}$$

$$E_{angle} = K_{angle}(\theta - \theta_0)^2 \tag{S5}$$

where K_{bond} *and* K_{angle} are the energy-related bond and angle coefficients, r_0 is the equilibrium bond distance, θ_0 is the equilibrium angle value.

The last term of the OPLS-AA force field is the torsion interaction, which is described by the *opls* dihedral style, as follows:

$$E(\phi) = \frac{V_1}{2}[1+\cos(\phi)] + \frac{V_2}{2}[1-\cos(2\phi)] + \frac{V_3}{2}[1+\cos(3\phi)] \tag{S6}$$

where V_1, V_2 and V_3 are the dihedral coefficients. The detailed parameters of OPLS-AA potential for decane molecules can be found in **Table S1**.

1.1.3 Force field parameters for ions

The potential parameters for sodium/chloride ions we used are the parameters reported by Lyubartsev *et al.*, [14] which are proved to be accurate and effective for simulating the structure and the dynamical properties of ions in the water phase.

Table S1. Force field parameters for water, decane and ions.

Water (TIP3P model) [11, 12]			
L-J potential parameters	σ (Å)	ε (10^{-3} eV)	charge (e)
O	3.188	4.423	−0.830
H	0	0	0.415
Bond potential parameters	K_{bond} (10^2 eV·Å^{-2})		r_0 (Å)
O-H	19.514		0.9572
Angle potential parameters	K_{angle} (eV·rad^{-2})		θ_0 (º)
H-O-H	2.385		104.52
Decane (OPLS-AA model) [13]			
L-J potential parameters	σ (Å)	ε (10^{-3} eV)	charge (e)
C, RCH_3	3.500	2.862	−0.180
C, R_2CH_2	3.500	2.862	−0.120
H	2.500	1.301	0.060

Bond potential parameters	K_{bond} (10^2 eV·Å^{-2})		r_0 (Å)
C-C	13.454		1.526
C-H	14.365		1.090
Angle potential parameters	K_{angle} (eV·rad^{-2})		θ_0 (º)
H-C-H	1.518		104.52
H-C-C	1.518		109.50
C-C-C	1.736		109.50
Dihedral potential parameters	V_1 (eV)	V_2 (eV)	V_3 (eV)
C-C-C-C	0.0755	−0.0068	0.0121
H-C-C-C	0	0	0.0159
H-C-C-H	0	0	0.0138
Ions [14]			
L-J potential parameters	σ (Å)	ε (10^{-3} eV)	charge (e)
Na^+	2.586	3.706	1
Cl^-	4.4015	1.740	−1

1.2 Simulation details

In this paper, the Nose-Hoover style non-Hamiltonian equations of motion [15, 16] are used to generate positions and velocities of atoms in the simulated system from the NPT ensembles. The equations of motion used in the simulations are those of Shinoda *et al*., [17] which combine the hydrostatic equations of Martyna *et al*. [18] with the strain energy proposed by Parrinello and Rahman. [19] The time integration schemes closely follow the time-reversible measure-preserving Verlet and rRESPA integrators derived by Tuckerman *et al*. [20] The T_{damp} parameter which determines how quickly the temperature relaxed is a value of 0.2 K, while the P_{damp} deciding the time scale on which pressure relaxed is a value of 1 ps. It is noteworthy that the good choice of the value of P_{damp} is about 1000 timesteps. If it is too small, the pressure and volume fluctuate severely; if it is too long, the equilibrium time for pressure is very long. In order to reduce the storage

requirements for the data analysis, the coordinates of the ions and molecules are output every 10000 timesteps, *i.e.* 1 ps.

Because of the charge properties of ions, the long-range Coulombic interactions between ions or molecules play an important role in the simulation systems. Thus, a solver to compute the long-range Coulombic interactions needs to be defined. In our simulations, we adopt the PPPM solver to calculate the long-range Coulombic force. This method uses 3d FFTs to solve Poisson's equation on the mesh which atom charge is mapped, then interpolates electric fields on the mesh points back to the atoms. The PPPM solver is a faster method to reduce the computation time and memory storage, because it scales as Nlog(N) where N is the total atom numbers, which is far less than the Ewald summation (N^(3/2)). The accuracy of PPPM method is 0.001 eV/Å and the grid of the mesh is 10 × 10 × 30 in the simulations. In our previous work, [10] we had compared a serials of number of grid mesh and verify that this grid size is rational to calculate the electrostatic interaction and improve computing efficiency.

1.3 Model validation

In order to illustrate the reasonableness and reliability of the simulation model and potential parameters, we had made a validation by comparing the simulated bulk densities or interfacial tension (IFT) with the actual value of them under the same conditions in our previous work. [9, 10] Therefore, we do not repeat it here. Different from previous models, we introduce an electric field which only applies external force on the ions to simulate the driving forces like surfactants for ions to transport across the interfaces. It is necessary to provide a discussion of the effects of electric field on the

simulation models. **Figure S1** shows the effects of electric field on the energies (kinetic energy, potential energy, E_coul and E_vdwl) of simulation system.

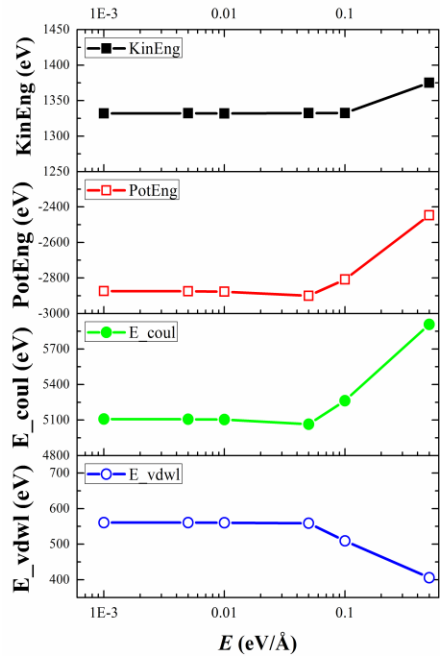

Figure S1. Variation of energies *versus* electric field intensity

As we can see from **Figure S1**, when the intensity of electric field *E* is smaller than 0.1 eV/Å, the variation of different energies is almost unchanged, which means that the electric field does not creates an unphysical system and the effects of electric field on the simulation results can be ignored. For specific electric field (*E*=0.1 eV/Å), the formation of water channel in the decane phase may induces a little change of the energies. However, the system is stable and the effects of electric field is also small. When *E*=0.5 eV/Å, single ions can easily transfer across the decane-water interfaces and finally break the stable interface systems. Therefore, the energies of systems under this electric field intensity show significant change.

2. Microstructures

2.1 Typical cases of ion transfer

In our simulations, we studied the ions transfer processes involving multiple ions at interfaces. Different from the case of single ions transfer across the interface, we found different evolution processes of the interfacial structures. **Figure S2** shows several typical cases during ions transfer across the interfaces under different ionic concentrations. At low ionic concentrations, a specific "water ridge" interfacial structure is found (Case 1), rather than the water finger. At high concentrations, different cases may occur. For Case 2, individual ion with a hydration shell transfer through the interface like the water finger of single ion across the interface. For Case 3, due to the interaction between ions at the interfaces, several ions successively transfer across the interface and form a more stable water finger with strong connectivity of water molecules.

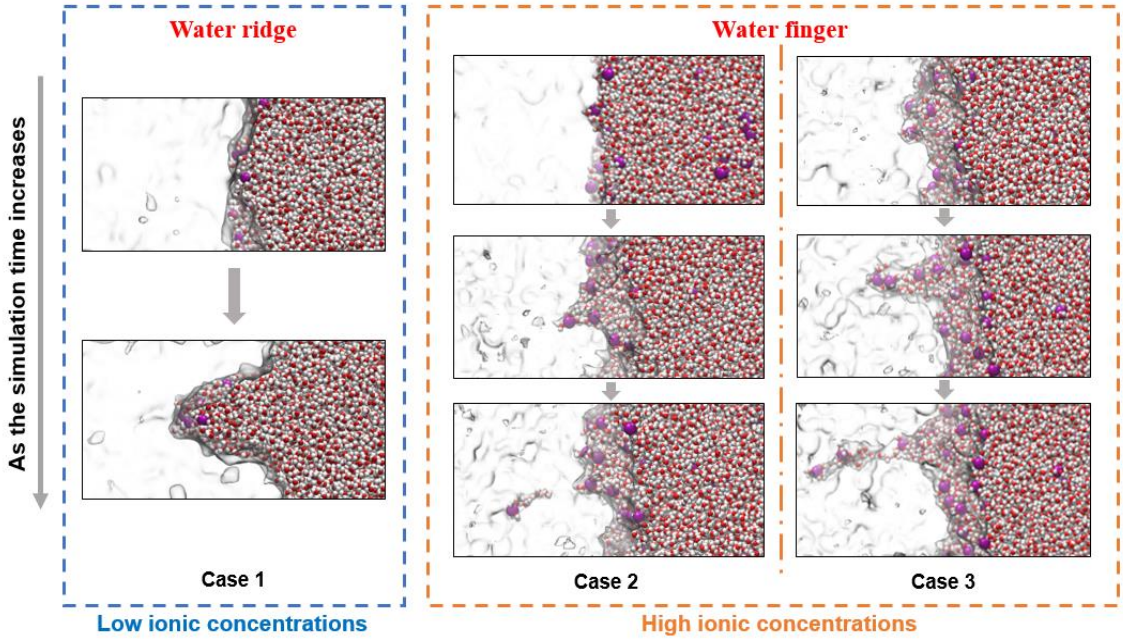

Figure S2. Different cases of ions transfer. (The glassblowing color: decane phase; purple: sodium ions; red: oxygen atoms; white: hydrogen atoms)

2.2 Water channel

Figure S3 shows the diagram of transport behaviors of ions across the decane-water interface under the effects of ionic concentrations and external forces. The transfer behaviors of ions across the interfaces are only related to the electric field applied on the ions. With the electric field intensity increasing, the sodium and chloride ions are separated gradually in the opposite direction and deposited at two decane-water interface separately. For low electric field intensity (E < 0.1 V/Å), ions are unable to transfer across the interfaces because the driving force generated by electric field cannot break through the barrier of interfaces. Particularly, the electric field (E < 0.01 V/Å) force even cannot separate the ion-pair formed by sodium and chloride ions. As the electric field intensity rises ($E \geq$ 0.1 V/Å), ions transport across the decane-water interface but only develop into a water channel in the decane phase under specific electric field intensity (E < 0.1 V/Å). The transfer modes and mechanism of ions across the interfaces are detailedly analyzed in the manuscript.

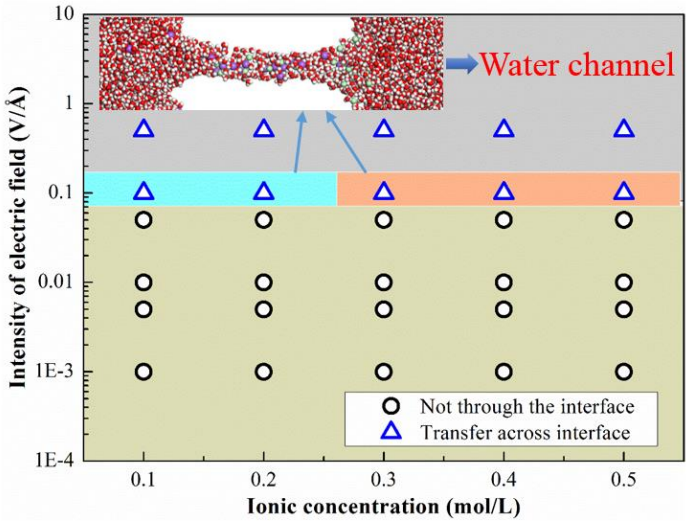

Figure S3. Phase diagram of ions transport across the interface and atomic view of water channel

Owing to the immiscibility between ions and decane phase, ions transfer across the interface and penetrate through the decane phase with the form of water channel, which is also mentioned in other literatures. Different from our "sandwich" simulation model, Qiao *et al.* [21] formulated a water-in-oil microemulsion model, in which a 5 nm diameter water is surrounded by oil molecules and ions are transported from water to the oil phase under the effect of extractants. In addition, Tang *et al.* [22] studied the detachment of a situated oil layer from the hydroxylated silica surface and found the water channel formation when the surfactants penetrate into the oil layer under the strong polar-interaction between surfactants and silica substrates. **Figure S4** shows the comparison of these simulation with our model. We may conclude that the formation of water channel is a specific phenomenon which has nothing to do with the simulation model and conditions, such as model size, boundary conditions, among others.

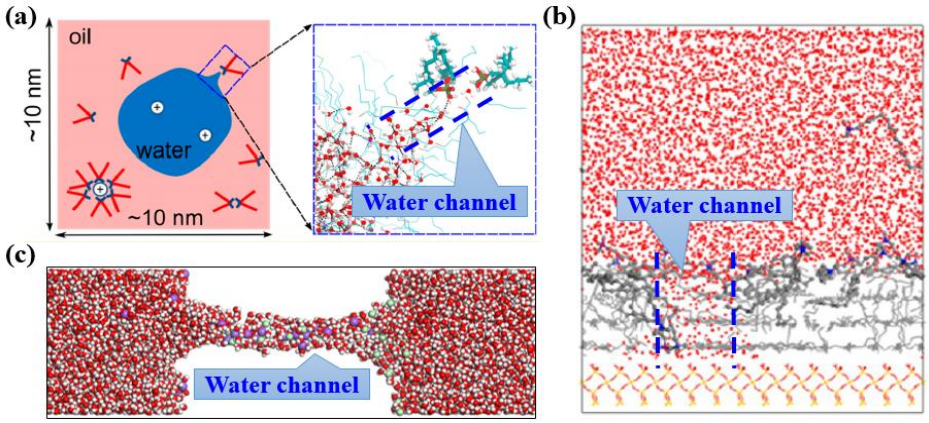

Figure S4. Comparison of simulation models. (a) Water-in-oil microemulsion model, from Ref. [13]; (b) Oil layer model at the solid surface, from Ref. [14]; (c) Our model.

Further, we give some quantitative description of the water channel, as shown in **Figure S5**. The diameter of water channel increases with ionic concentration rising. In order to analyze how characteristics of water channel change with ionic concentration,

we propose two geometric parameters: D and D', which stand for diameters of water channel and ion distribution area respectively (see **Figure S5(b)**). Since the size of water channel is not uniform across the decane phase and fluctuates as a function of time, these parameters are obtained by calculating the time-averaged diameters of water channel along z-direction. The maximum diameter of O and H atoms distributing at the water channel is named D while the maximum diameter of ions distributing at the water channel is called D'. The time-averaged percentage distributions of atoms at water channel show that the ions tend to distribute at the central region of water channel because of their hydration. **Figure S5(c)** displays the D and $D-D'$ *versus* ionic concentration. With ionic concentration increasing, the diameter of water channel D increases sharply and then tends to a certain value while the value of $D-D'$ shows upward trend with a characteristic stage. At low ionic concentration (c= 0.1 and 0.2 mol/L), the values of $D-D'$ are roughly equal to 5~6 Å, which are about twice the diameter of water molecule (≈3 Å). It means that there is at least one layer of water molecules between the decane phase and ions at the water channel. At high ionic concentrations (c > 0.2 mol/L), the values of $D-D'$ are approximately 8~9 Å, which are about three times the diameters of water molecule due to more water molecules carried by ions. We attribute the variation of $D-D'$ to the change of water molecule conformation at water channel near the decane phase. **Figure S5(d)** compares the water conformation at c = 0.1 mol/L and c = 0.5 mol/L. The parameter θ, which is the angle between interface and direction of the water dipole moment, is adopted to describe the water conformation. At low ionic concentrations, more water molecules are perpendicular to the interface. With ionic concentration

increasing, a weakening trend of water molecules perpendicular to the interface occurs. The distribution of angle θ is more dispersed, inducing an increase of the thickness D–D'.

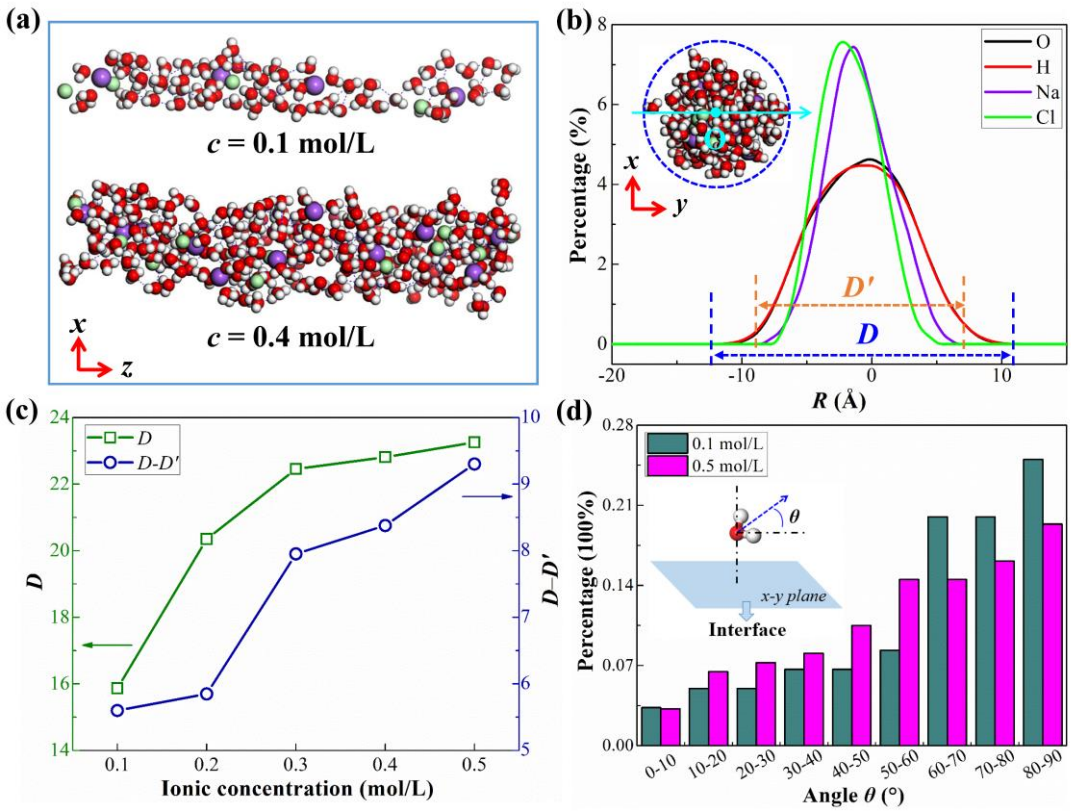

Figure S5. Characteristics of water channel. (a) Atomic views of water channel (c = 0.1 and 0.4 mol/L); (b) Percentage distributions of atoms along the radial direction at water channel (c = 0.5 mol/L); (c) D and D–D' *versus* ionic concentration; (d) The angle θ distributions (c = 0.1 and 0.5 mol/L).

2.3 Density distribution

Figure S6 shows the density distributions of water, decane and ions along z-direction in cases under c=0.5 mol/L, E=0.01 V/Å condition. We use the following hyperbolic tangent function to fit the density distribution profiles of the water and decane molecules.

$$\rho_i(z) = \frac{\rho_{i,bulk}}{2} - \frac{\rho_{i,bulk}}{2}\tanh\left(\frac{2(z-z_0)}{d}\right) \tag{S7}$$

where ρ_i is the density, z_0 is the position of the Gibbs interface, d is the alterable parameter concerning with the interfacial thickness. The interfacial thickness is defined as the distance between the positions where the densities of water or decane respectively reach the 90% of their bulk densities, which are shown in the baby blue region of **Figure S6**. It is a common practice to determine the interfacial thickness of the liquid-vapor or liquid-liquid interface.

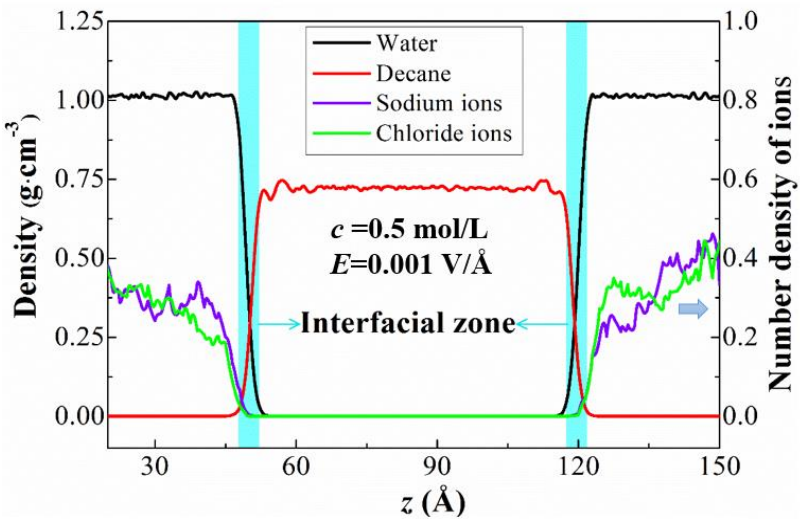

Figure S6. Density distributions of water, decane and ions (number density) along *z*-direction under *c*=0.5 mol/L, *E*=0.001 V/Å condition

In the manuscript, we detailedly discuss the density distribution of ions with ionic concentration or electric field intensity increasing. Here, we perform a supplementary analysis on the density distribution of water and decane molecules along *z*-direction under *E*=0.001 eV/Å or *c*=0.5 mol/L conditions, as shown in **Figure S7**. With the intensity of electric field increasing, more ions aggregate at the decane-water interfaces and induce a slight decrease of the water and decane densities at the interface, therefore widening the interfacial thickness. With ionic concentration rising, the interfacial thickness remains nearly constant but the interfacial area shifts towards the water phase.

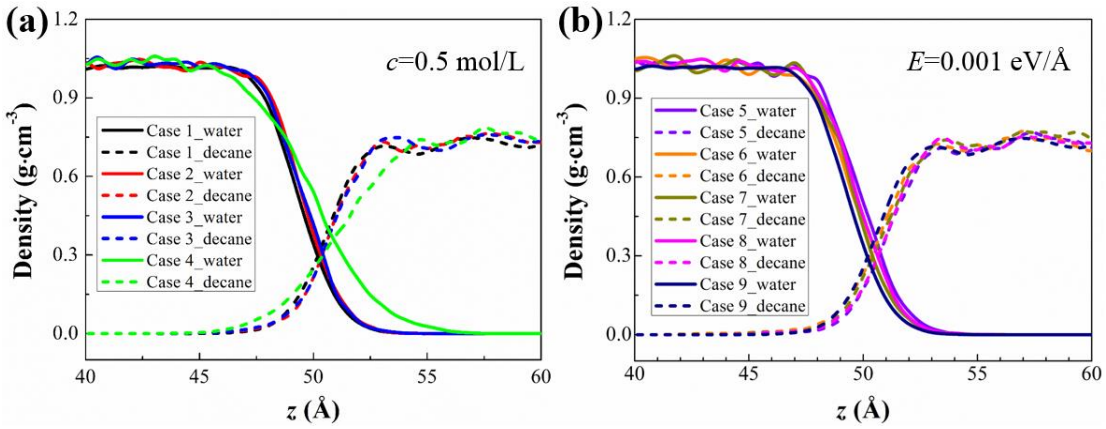

Figure S7. Density distribution of water and decane molecules. (a) Density distribution along *z*-direction *vs.* electric field intensity: Case 1-4: *c*=0.5 mol/L, *E*=0.001, 0.005, 0.01 and 0.05 eV/Å, orderly; (b) Density distribution along *z*-direction *vs.* ionic concentration: Case 5-9: *E*=0.001 eV/Å, *c*=0.1, 0.2, 0.3, 0.4 and 0.5 mol/L, successively.

We also found that the adsorption behavior of ions at the interface is a dynamic process, which is accompanied by the desorption and diffusion of ions at the same time. As shown in **Figure S8**, ions move back and forth between the water phase and the interface. The adsorption sites of ions at interface are always changing.

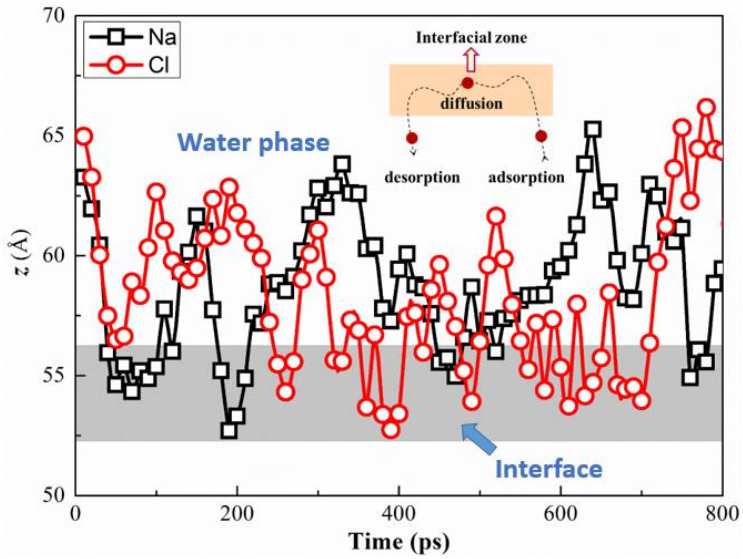

Figure S8. The variation of *z* coordinate for specific ion *versus* simulation time.

2.4 Interfacial thickness

Based on the **Equation (S7)**, we can obtain the interfacial thickness of the decane-water interface systems with different ion concentrations or electric field intensities under specific conditions. **Figure S9** shows how the interfacial thickness of the decane-water interface change with electric field intensity or ionic concentration increasing. At the ion concentration of 0.5 mol/L, the interfacial thickness slightly increases as the intensity of electric field rises, which is attributed to the aggregation of more ions at the decane-water interfaces. In addition, with ion concentration rising, the interfacial thickness remains almost unchanged under *E*=0.001 mol/L condition. To our knowledge, the larger interfacial thickness means the stronger miscibility, therefore inducing a smaller interfacial thickness.

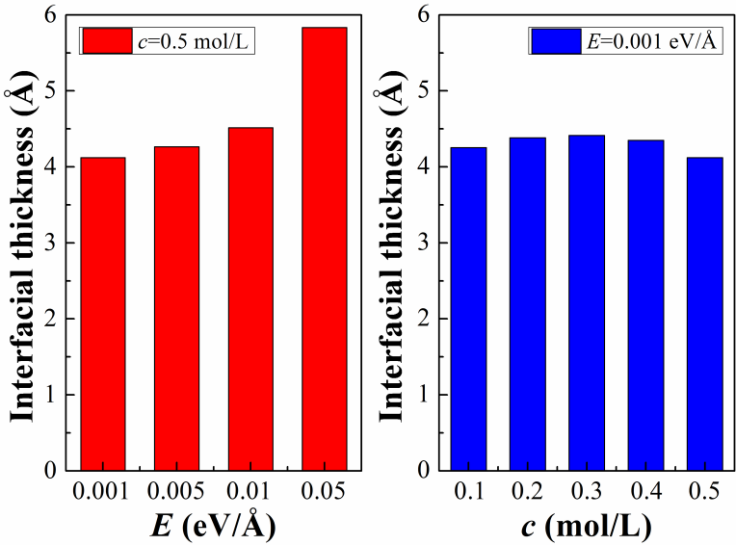

Figure S9. Interfacial thickness. (a) Interfacial thickness *vs.* electric field intensity: *c*=0.5 mol/L; (b) Interfacial thickness *vs.* ionic concentration: *E*=0.001 eV/Å.

References

1. W. L. Jorgensen, J. Chandrasekhar, J. D. Madura, R. W. Impey and M. L. Klein, *J. Chem. Phys.*, 1983, **79**, 926-935.
2. P. Mark and L. Nilsson, *J. Phys. Chem. A*, 2001, **105**, 9954-9960.
3. C. Vega, J. L. F. Abascal, E. Sanz, L. G. Macdowell and C. Mcbride, *J. Phys-Condens. Mat.*, 2005, **17**, S3283-S3288.
4. J. Zielkiewicz, *J. Chem. Phys.*, 2005, **123**, 1545.
5. C. Feng and P. E. Smith, *J. Chem. Phys.*, 2007, **126**, 4873.
6. Q. Ji, J. M. Pellenq and K. J. V. Vliet, *Comput. Mater. Sci.*, 2012, **53**, 234-240.
7. D. J. Huggins, *J. Chem. Phys.*, 2012, **136**, 851.
8. T. Yagasaki, M. Matsumoto and H. Tanaka, *J. Phys. Chem. B*, 2018, **122**, 7718-7725.
9. B. Wen, C. Sun, B. Bai, E. Y. Gatapova and O. A. Kabov, *Phys. Chem. Chem. Phys.*, 2017, **19**, 14606-14614.
10. B. Wen, C. Sun and B. Bai, *Phys. Chem. Chem. Phys.*, 2018, **20**, 22796-22804.
11. W. L. Jorgensen, J. Chandrasekhar, J. D. Madura, R. W. Impey and M. L. Klein, *J. Chem. Phys.*, 1983, **79**, 926.
12. S. L. Price, A. J. Stone and M. Alderton, *Mol. Phys.*, 1984, **52**, 987-1001.
13. S. W. I. Siu, K. Pluhackova and R. A. Böckmann, *J. Chem. Theory Comput.*, 2012, **8**, 1459-1470.
14. A. P. Lyubartsev and A. Laaksonen, *J. Phys. Chem.*, 1996, **100**, 16410-16418.
15. S. Nosé, *Mol. Phys.*, 1984, **52**, 255-268.
16. W. G. Hoover, *Phys. Rev. A-Gen. Phys.*, 1985, **31**, 1695-1697.
17. W. Shinoda, M. Shiga and M. Mikami, *Phys. Rev. B*, 2004, **69**, 134103.
18. G. J. Martyna, D. J. Tobias and M. L. Klein, *J. Chem. Phys.*, 1994, **101**, 4177-4189.
19. M. Parrinello and A. Rahman, *Phys. Rev. Lett.*, 1980, **45**, 1196-1199.
20. M. E. Tuckerman, J. Alejandre, R. López-Rendón, A. L. Jochim and G. J. Martyna, *J. Phys. A- Gen. Phys.*, 2006, **39**, 5629.
21. B. Qiao, J. V. Muntean, M. Olvera de la Cruz and R. J. Ellis, *Langmuir*, 2017, **33**, 6135-6142.
22. J. Tang, Z. Qu, J. Luo, L. He, P. Wang, P. Zhang, X. Tang, Y. Pei, B. Ding, B. Peng and Y. Huang, *J. Phys. Chem. B*, 2018, **122**, 1905-1918.